

## Machine learning-assisted high-content analysis of pluripotent stem cell-derived embryos *in vitro*

Jiaying Guo,<sup>1,2,6</sup> Peizhe Wang,<sup>1,6</sup> Berna Sozen,<sup>3,4</sup> Hui Qiu,<sup>1,2</sup> Yonglin Zhu,<sup>1</sup> Xingwu Zhang,<sup>1</sup> Jia Ming,<sup>1</sup> Magdalena Zernicka-Goetz,<sup>3,5,\*</sup> and Jie Na<sup>1,\*</sup>

<sup>1</sup>Center for Stem Cell Biology and Regenerative Medicine, School of Medicine, Tsinghua University, Beijing 100084, China

<sup>2</sup>Tsinghua-Peking Center for Life Sciences, 100084 Beijing, China

<sup>3</sup>Mammalian Embryo and Stem Cell Group, Department of Physiology, Development and Neuroscience, University of Cambridge, Downing Street, Cambridge, CB2 3DY, UK

<sup>4</sup>Department of Genetics, School of Medicine, Yale University, New Haven, CT 06510, USA

<sup>5</sup>California Institute of Technology, Division of Biological Engineering, 1200 E. California Boulevard, Pasadena, CA 91125, USA

<sup>6</sup>These authors contributed equally

\*Correspondence: [mz205@cam.ac.uk](mailto:mz205@cam.ac.uk) (M.Z.-G.), [jie.na@tsinghua.edu.cn](mailto:jie.na@tsinghua.edu.cn) (J.N.)

<https://doi.org/10.1016/j.stemcr.2021.03.018>

### SUMMARY

Stem cell-based embryo models by cultured pluripotent and extra-embryonic lineage stem cells are novel platforms to model early post-implantation development. We showed that induced pluripotent stem cells (iPSCs) could form ITS (iPSCs and trophectoderm stem cells) and ITX (iPSCs, trophectoderm stem cells, and XEN cells) embryos, resembling the early gastrula embryo developed *in vivo*. To facilitate the efficient and unbiased analysis of the stem cell-based embryo model, we set up a machine learning workflow to extract multi-dimensional features and perform quantification of ITS embryos using 3D images collected from a high-content screening system. We found that different PSC lines differ in their ability to form embryo-like structures. Through high-content screening of small molecules and cytokines, we identified that BMP4 best promoted the morphogenesis of the ITS embryo. Our study established an innovative strategy to analyze stem cell-based embryo models and uncovered new roles of BMP4 in stem cell-based embryo models.

### INTRODUCTION

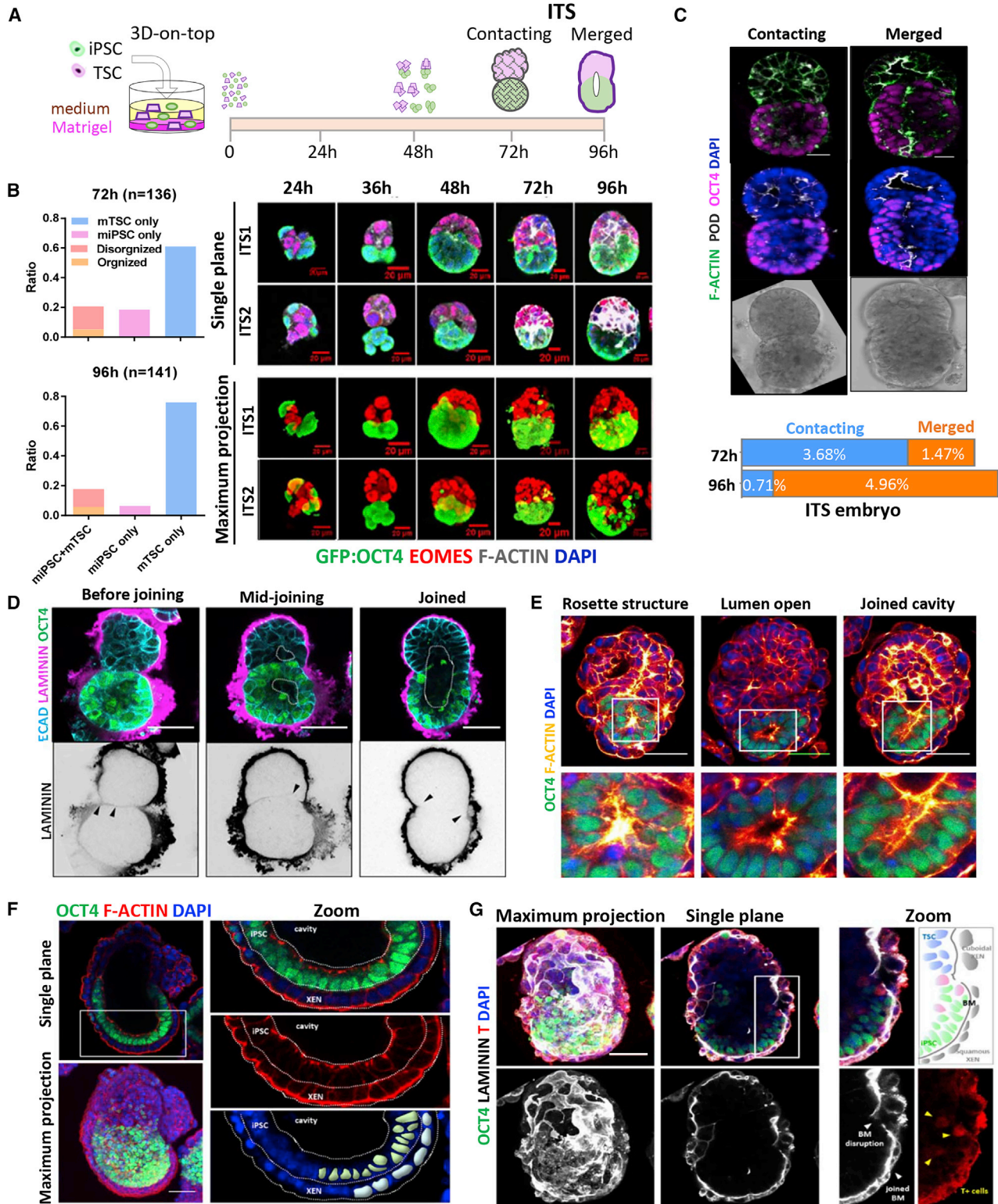
During early mammalian postimplantation development, the primary germ layers are specified, and the body axes are determined. Due to the nature of the *in utero* development and the small size, it is challenging to study gastrula stage embryos. Remarkably, stem cell lines derived from the early mammalian embryo can be propagated for long-term *in vitro*, while retaining many essential properties of their *in vivo* counterpart. In recent years, several groups have shown that embryonic stem cells (ESCs) and extra-embryonic (ExE) stem cell lines can self-assemble to form embryo-like structures and recapitulate various aspects of the peri- and postimplantation embryo development *in vitro* (Beccari et al., 2018; Bedzhov and Zernicka-Goetz, 2014; Harrison et al., 2017; Li et al., 2019; Poh et al., 2014; Rivron et al., 2018; Shao et al., 2017a; Sozen et al., 2018, 2019; Veenvliet et al., 2020; Zhang et al., 2019). These stem cell-based embryo models are amenable to microscope observation and experimental manipulation, opening up a new venue to investigate the spatiotemporal regulation of morphogenesis and cell fate specification, to discover the complex embryological events and mechanisms. Moreover, the *in vitro* platform greatly facilitated the study of human embryo development (Deglincerti et al., 2016; Shahbazi et al., 2016; Shao et al., 2017a, 2017b; Zheng et al., 2019). Analyses of previous stem cell-based embryo models are mostly based on manual identification of the

representative morphology. The drawback is low efficiency and non-standardized means and parameters used by different researchers. Moreover, pluripotent stem cells (PSCs) are known for variations across cell lines depending on the genetic background, the derivation, culture, and reprogramming methods. Therefore, an automated, high-throughput, multi-dimensional, and unbiased workflow to quantitatively analyze stem cell-based embryo models is needed.

High-throughput and high-content imaging and analysis have been used for drug screens on cell-based assays. In recent years, the capacity for imaging acquisition and processing has increased dramatically. More and more machine learning algorithms to analyze complex and high-dimensional images have been developed (Boutros et al., 2015; Lukonin et al., 2020; Scheeder et al., 2018; Shen et al., 2018). These advances have enabled automated screens on 3D organoid systems. Czerniecki et al. (2018) showed that it is possible to perform high-throughput, high-content screening (HSC) on human PSC (hPSC)-derived kidney organoids in an automated manner. Compared with the kidney organoid, stem cell-based embryo models are independent 3D structures with a defined size and more sophisticated morphology. Therefore, they represent a different challenge for high-content imaging analysis.

In this study, we set up a workflow to use machine learning-assisted high-content analysis to study





(legend on next page)



embryo-like structures derived from several mouse induced pluripotent stem (iPSC) lines and embryonic stem cells (ESCs). Using this system, we optimized the culture condition, screened 55 small molecules and cytokines, and found that BMP4 is the best candidate to facilitate the formation and the development of the iPSCs and trophoblast stem cell (ITS) embryos. Our study provides an innovative strategy to improve the efficiency and unbiased multi-dimensional analysis of stem cell-based embryos.

## RESULTS

### Self-assembly of mouse iPSCs, TSCs, and XEN cells into postimplantation embryo-like structures

When cultured together, mouse embryonic and ExE stem cells can spontaneously organize into structures that closely resemble the early postimplantation stage mouse embryo (Harrison et al., 2017; Sozen et al., 2018). To replicate this process with mouse iPSCs, we mixed D9-iPSCs (Liu et al., 2018) with trophoblast stem cells (TSCs) using the 3D-on-top Matrigel condition as described in (Harrison et al., 2017, 2018) (Figure 1A). By 72 h, some iPSC aggregates formed postimplantation embryo-like structures with TSC aggregates, which we refer to as ITS embryos (Figure 1B). Visual inspection counted less than 20% aggregates containing both iPSCs and TSCs. An ITS embryo with postimplantation embryo morphology only comprises about 5% of total aggregates (Figure 1B). In some ITS embryos, F-actin concentrated at the iPSC compart-

ment center, a hallmark for polarized epiblast cells. Based on the pattern of F-actin and podocalyxin staining, we classify ITS embryos as "contacting" or "merged" (Figure 1C). The merged ITS embryos have a pro-amniotic cavity at the center of iPSC and TSC compartments, and hence are considered to be in a more advanced developmental stage than contacting-stage ITS embryos. From 72 to 96 h, the percentage of contacting ITS embryos decreased from 3.68% to 0.71%, while the percentage of merged embryos increased from 1.47% to 4.96% (Figure 1C). In accordance with the morphology change, a thin but clear laminin boundary initially formed between iPSC and TSC compartments in contacting ITS embryos (Figure 1D, left panel), then began to degrade when the two compartments continued to merge (Figure 1D, middle panel). Once the pro-amniotic cavity forms, the laminin boundary between the two compartments disappeared entirely, with only the continuous laminin layer surrounding the outside of the ITS embryo remaining (Figure 1D, right panel).

Next, we added extraembryonic endoderm stem (XEN) cells to generate ITX (iPSCs, trophoblast stem cells, and XEN cells) embryos with a visceral endoderm layer (Figure S1A); 108 h after mixing, 8.9% structures formed postimplantation embryo-like ITX embryos containing cells from the three lineages. The embryonic compartment contained highly polarized OCT4+ epiblast (EPI) cells and have bright F-actin signal concentrated toward the pro-amniotic cavity (Figures 1E–1F, and S1B–S1E). XEN cells are also polarized with strong F-actin lining the outer membrane, forming a smooth contour of the ITX embryo

### Figure 1. Self-assembly of mouse iPSCs, TSCs, and XEN cells into postimplantation embryo-like structures

(A) Schematic of the 3D-on-top protocol to generate mouse ITS (iPSCs + TSC) embryos and representative examples of ITS embryo, iPSC-alone, and TSC-alone structures during 4 days of culture. Green, OCT4 of iPSC compartment; red, EOMES of TSC compartment; white, F-actin showing cell shape; blue, DAPI.

(B) Example and frequency of iPSC-alone, TSC-alone, and ITS embryos at 72 h ( $n = 136$  ITSs from 3 separate experiments) and 96 h ( $n = 141$  ITSs from 3 separate experiments). Clones containing both iPSCs and TSCs with morphology similar to that shown on the right were classified as ITS embryos (contacting or merged); other atypical clones with two cell types were counted as disorganized. Scale bars, 20  $\mu\text{m}$ .

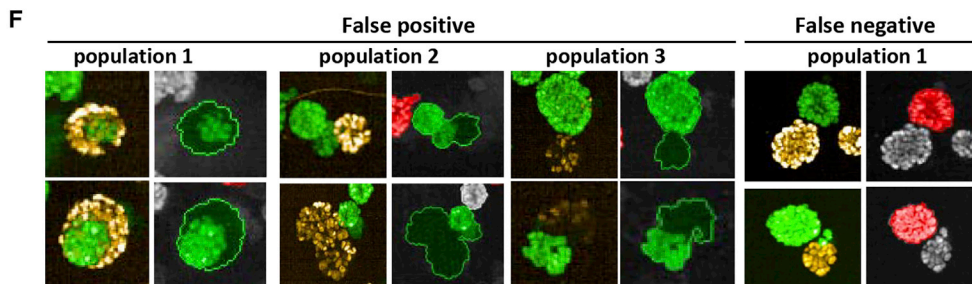
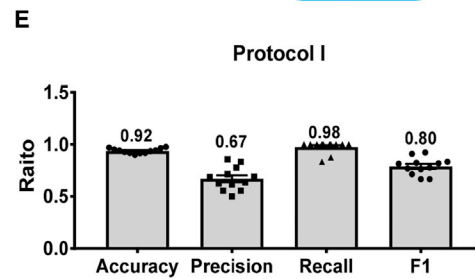
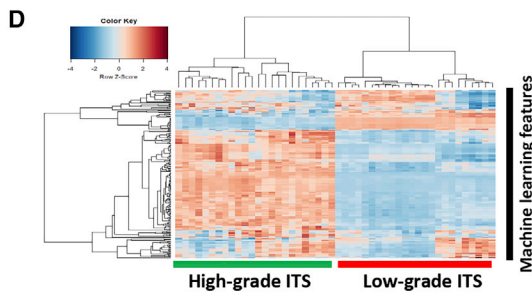
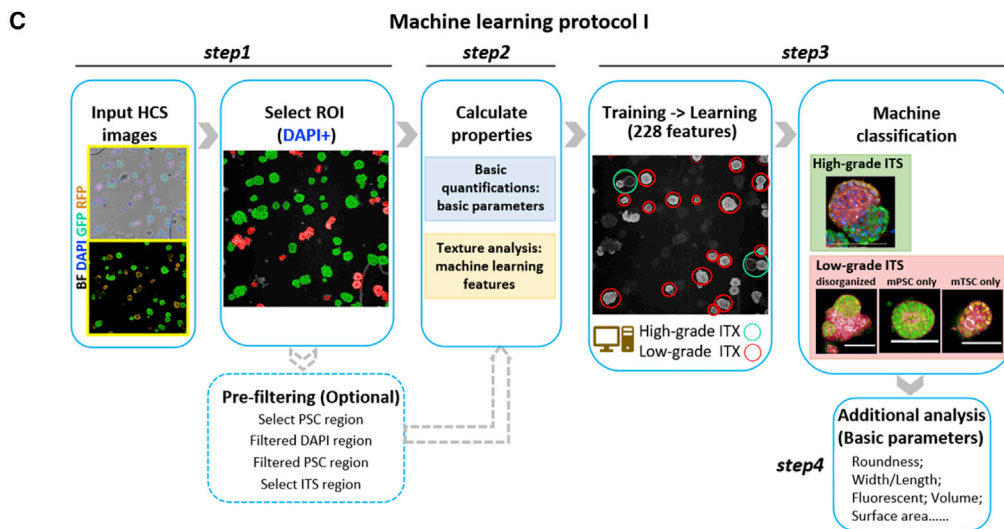
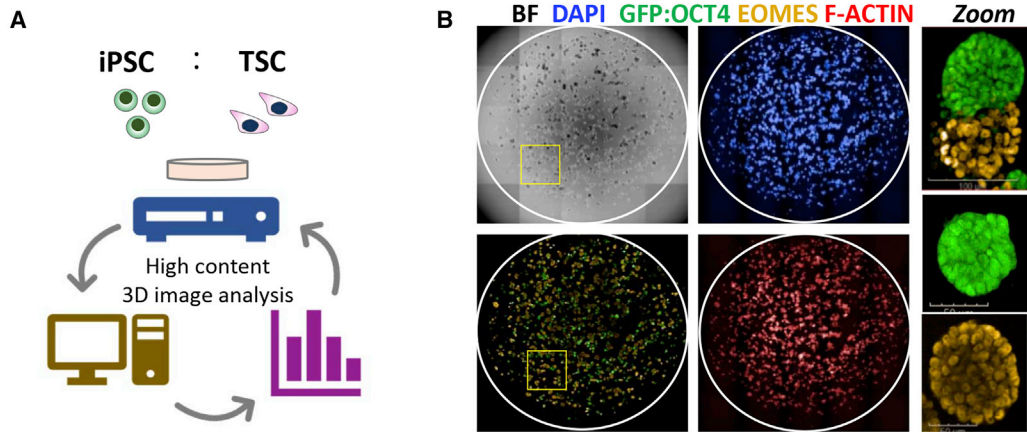
(C) Example and frequency of contacting and merged ITS embryos at 72 and 96 h ( $n = 141$ ). Green, F-actin showing cell shape; white: podocalyxin showing cell polarization; pink, OCT4 showing iPSC compartment; blue, DAPI. Scale bars, 20  $\mu\text{m}$ . The percentage of contacting or merged ITS embryos at 72 h ( $n = 136$  ITSs from 3 separate experiments) and 96 h ( $n = 141$  ITSs from 3 separate experiments) is below the images.

(D) Example of ITS embryos. Upper panels are immunostaining images showing the merging cavity in ITS embryos. Light blue, E-cadherin showing cell shape; pink, laminin; green, OCT4. Scale bars, 20  $\mu\text{m}$ . Lower panels are the greyscale image of the laminin staining. Black arrowheads indicate the disappearing laminin boundary between iPSC and TSC compartments.

(E) Series of images showing lumen emergence in ITX embryos. Left panel, polarized iPSCs form a rosette pattern; middle panel, a small lumen opens in the iPSC part; right panel, a joined pro-amniotic cavity connects the iPSC and TSC compartments. Green, OCT4 showing iPSC compartment; yellow, F-actin showing the cell shape and polarity; blue, DAPI.  $n = 30$  ITSs from 3 separate experiments. Scale bars, 20  $\mu\text{m}$ .

(F) An ITX embryo with an expanded amniotic cavity-like lumen and polarized epithelium. Green, OCT4 showing iPSC parts; red, F-actin showing cell shape; blue, DAPI. Scale bar, 20  $\mu\text{m}$ .

(G) A typical ITX embryo with basement membrane (BM) surrounding the joined iPSC-TSC compartments. White arrows indicate BM; yellow arrows indicate T/brachyury-expressing cells in the iPSC compartment. Right panels, XEN cells adjacent to iPSCs and TSCs have distinct shapes. Green, OCT4; white, laminin; red, T; blue, DAPI. Scale bar, 20  $\mu\text{m}$ .



(legend on next page)



(Figure 1F). In 26.67% of ITX embryos, T-expressing iPSCs localize to one side of the embryo, where the basement membrane between XEN cells and EPI started to disappear (Figures 1G and S1F–S1H). Thus, iPSCs can coordinate with TSC and XEN cells to form ITX embryos, break symmetry, and initiate mesoderm formation.

### Machine learning-assisted high-content analysis of ITS embryos

The morphological traits of stem cell-based embryos were often manually scored, which is time consuming and may introduce bias. To avoid such problems, we used an HCS system to capture ITS 3D images in 48-well plates (Figures 2A and 2B). Then we set up a supervised machine learning protocol I (see supplemental information for details about PhenoLOGIC machine learning algorithms) to classify ITS embryos based on HCS images and perform multi-trait analysis (Figure 2C). The machine learning algorithms developed by the PerkinElmer HCS system are based on a compilation of texture analysis algorithms that can extract hundreds of features, such as the symmetric distribution and compactness of the staining, profiles that subdivide the cells into different zones. As the features extracted by the machine learning algorithms lack clear biological meaning, we also performed additional quantification of basic parameters, so-called spot properties, such as area, roundness, length, width, fluorescence intensity, etc., that have a clear biological meaning. A machine learning protocol is an analysis sequence that includes multiple “building blocks.” Each building block can be an image processing step, such as “select all DAPI + regions,” “training-machining learning modules,” or “quantification of basic parameters.” But there can be only one machining learning module in an analysis sequence.

The HCS image series with bright-field, DAPI, GFP, and RFP channels were the input images. We used DAPI staining to select regions of interest (ROIs) for subsequent analysis. Before starting training and machine learning

analysis, the researcher can perform an optional pre-filtering step to rule out poor-quality ROIs, thus reducing the total number of ROIs need to be analyzed and saving some computing time. Then we selected structures with good morphology as high-grade ITS examples (green circles), and structures that do not look like ITS embryos as low-grade ITS examples (red circles), and used them to train the machine learning algorithms until the goodness parameter reached above 1 (Figures 2C and S2A–S2C). High-grade ITS examples have embryonic and ExE parts with uniform OCT4 and EOMES staining, and are in contact with each other. In contrast, all other structures were defined as low-grade ITS examples, including disorganized, mPSC, or mTSC-alone structures (Figure 2C, step 3). After training, machine learning protocol I extracted a total of 228 multivariate features with 4 of them weighted most (Figure S2E) that can separate high- and low-grade ITS examples (Figure 2D). To validate machine learning protocol I, we compared the result given by machine learning algorithms with the analysis result by an experienced researcher, and the outcome was highly consistent (Figure S2D) with an accuracy of 0.92 and F1 score of 0.80 (Figures 2E and S2F). Examples of the false positive (incorrectly classified) ITSs shown in Figure 2F include three subpopulations, while a negligible percentage (0.21%) of high-grade ITSs were identified as false negative due to the filtering and gating threshold. These misclassifications can be further reduced by changing the pre-filtering parameters, increasing input training samples, or setting up more training classes.

We next used machine learning protocol I to determine the best starting cell ratio to form ITS embryos. TSCs and iPSCs were mixed at a ratio ranging from 3:1 to 1:6 (Figure S3A). The high-grade ITS ratio is the highest when TSC:iPSC ratio is 1:1 (Figure S3B). Only the mean fluorescent intensity (MFI) of OCT4 and EOMES, but not other basic parameters, were affected by different TSC:iPSC ratios (Figure S3C). Thus, the HCS system, combined with machining learning-assisted 3D image analysis, enabled

### Figure 2. Machine learning protocol I for analyzing ITS embryos

(A) Schematic of setting up the HCS system-based ITS embryo experiment.

(B) Examples of scanned images by PerkinElmer Opera Phenix high-content confocal. Each well view is combined from 25 fields. BF, bright field; green, OCT4 of iPSC compartment; yellow, EOMES of TSC compartment; red, F-actin showing cell shape and polarity; blue, DAPI. The zoomed ITS, iPSC-alone, and TSC-alone structures. Scale bars, 50  $\mu\text{m}$ .

(C) Schematic of HCS data analysis strategy based on machine learning protocol I. Step 1, the green structures were selected regions for downstream analyses; red structures were filtered regions excluded for analysis. Step 2, calculate parameters: including basic parameters or texture analysis extracted features. Step 3, the green or red circles mark the input-high or low-grade ITS examples for training, respectively. Step 4 (optional), high-grade ITSs were further characterized by basic parameters.

(D) Heatmap showing 228 machine learning features used to separate high-grade ITS and low-grade ITS.

(E) Evaluation of the performance of machine learning protocol I. The value of accuracy, precision, recall, and F1 are indicated.

(F) Representative images of the false-positive and false-negative examples of machine learning protocol I. Green- and red-stained structures are high- and low-grade ITS recognized by machine learning;  $n = 1,189$  from 12 independent wells.



automated and unbiased identification of favorable conditions for stem cell-based embryo or organoid generation.

### Machine learning-assisted high-content analysis of polarization capacity

Different PSC lines may differ in their ability to form embryo-like structures. Since polarization is the key indication of better-developed ITSs, we set up machine learning protocol II (see [supplemental information](#) for algorithms about machine learning) to classify highly polarized structures and quantify polarity-related machine learning features/basic parameters (Figure 3A). F-actin staining was used to detect polarized (rosette) and non-polarized (non-rosette) embryoid bodies (EBs) from PSCs cultured in 3D (Figure 3B). EBs with or without an F-actin ring were recognized as rosette or non-rosette, and the goodness parameter reached 1.35 (Figures S4A and S4B). Machine learning protocol II initially extracted 204 features, with 8 of them being key features for the separation (Figures 3C and S4C). After checking 8 independent wells of PSC aggregates for different rosette/non-rosette ratios, the accuracy of correct classification reached 0.81, and the F1 score was 0.69 (Figure 3D). The false-positive and false-negative classifications were mainly because of the ambiguous phenotypes, which were hard to define and cannot be clearly judged by the human eye (Figure 3E). More precise representative samples need to be used for training or else use unsupervised machine learning to cluster all different phenotypes to solve this problem. After analyses by machine learning protocol II, we found that different iPSCs and ESCs differed in their abilities to form polarized EBs (Figure 3F).

### Evaluating different mouse PSC lines by multi-parameters

Next, we used the HCS system to evaluate different PSC lines. We collected four iPSC lines (D9, OG2, MHC, and 2-iPS-32) generated by different reprogramming methods and four ESC lines (46C, V6.5, R1, and E14T) from different genetic backgrounds (Table S6). When cultured on feeder cells, the number, solidity, and roundness of the colony from the above PSC lines were similar. In contrast, the total area and average size of the colony differ from one another (Figures 4A and 4B).

Since each analysis sequence can insert only one machine learning-based building block in our system, we next did a statistical analysis of the 204 machine learning features and 14 basic parameters analyzed by machine learning protocol II to seek the most relevant parameters to quantify the polarization capacity. After the quantification and significance analysis, values from 5 basic parameters (area, F-actin sum, F-actin CV, F-actin SD, F-actin max), and 39 machine learning features can separate rosette and non-rosette EBs (Figures 4C–4E). The 5 basic parameters

that showed significant differences between rosette and non-rosette structures were subsequently used to quantify the polarization capacity of 3D cultured structures.

To automatically compare the ITS formation capacities of different PSC lines at a multi-parameters level, machine learning protocol I was used for the separation of high- and low-grade ITSs, then the five basic parameters recognized by machine learning protocol II would quantify which condition can give rise to more high-grade ITS embryos with polarized epiblast cells (Figure S4D). Other parameters, such as the number/ratio of high-grade ITS and the OCT4/EOMES MFI were also considered. We then analyzed ITS and ETS (embryo-like structures generated from ESCs and TSCs) embryos assembled from the eight different PSC lines. D9 iPSC line and V6.5 ESC line gave the best high-grade ITS/ETS embryo numbers and ratio; 2-iPS-32 and D9 iPSC lines, R1, and E14T ESC lines showed better polarization; ITS embryos generated from 2-iPS-32 iPSC line had the highest TSC quality as measured by EOMES MFI; ETS embryos with OG2 ESC line displayed the highest OCT4 MFI due to the GFP expression drive by the Oct4 promoter; ITS/ETS embryos formed from other PSC lines had comparable levels of OCT4 and EOMES MFI (Figures 4F and S4E–S4G). Thus, machine learning-assisted HCS may provide an efficient and non-biased method to compare different PSC lines regarding their potential to form proper ITS/ETS embryos.

### HCS of small molecules and cytokines identified BMP4 as a potent inducer of ITS/ETS embryo morphogenesis

As small molecules and cytokines can significantly affect stem cell differentiation potential, we conducted a screen of 55 small molecules and protein factors based on their known effect on early embryo and PSC survival, self-renewal, and differentiation (Table S7). The screening procedure is illustrated in Figure 5A. After small-molecule treatment, ITS embryos were fixed and stained for DNA, EOMES, and F-actin. An example of 3D images of ITS embryos acquired by the HCS system is shown in Figure 5B (Video S1–S5). We used the machine learning analysis sequence to systematically quantify polarized high-grade ITS embryos (Figure 5C). Twenty-three out of 55 compounds increased the number and ratio of high-grade ITSs compared with the DMSO control (Figure 5D). Twelve out of 55 compounds increased the quality of iPSCs and TSCs (Figure 5E). Previous research suggested that a rosette-like epiblast predicts better development of the stem cell-based embryo, so we defined a metric for calculating polarity score based on the fold change and p value of the five polarity parameters from our significance analysis (Figures 4D and S5A). Thirty-six out of 55 compounds increased the polarization scores of the ITSs (Figure 5F). After the primary screen, seven candidates (A1210477,

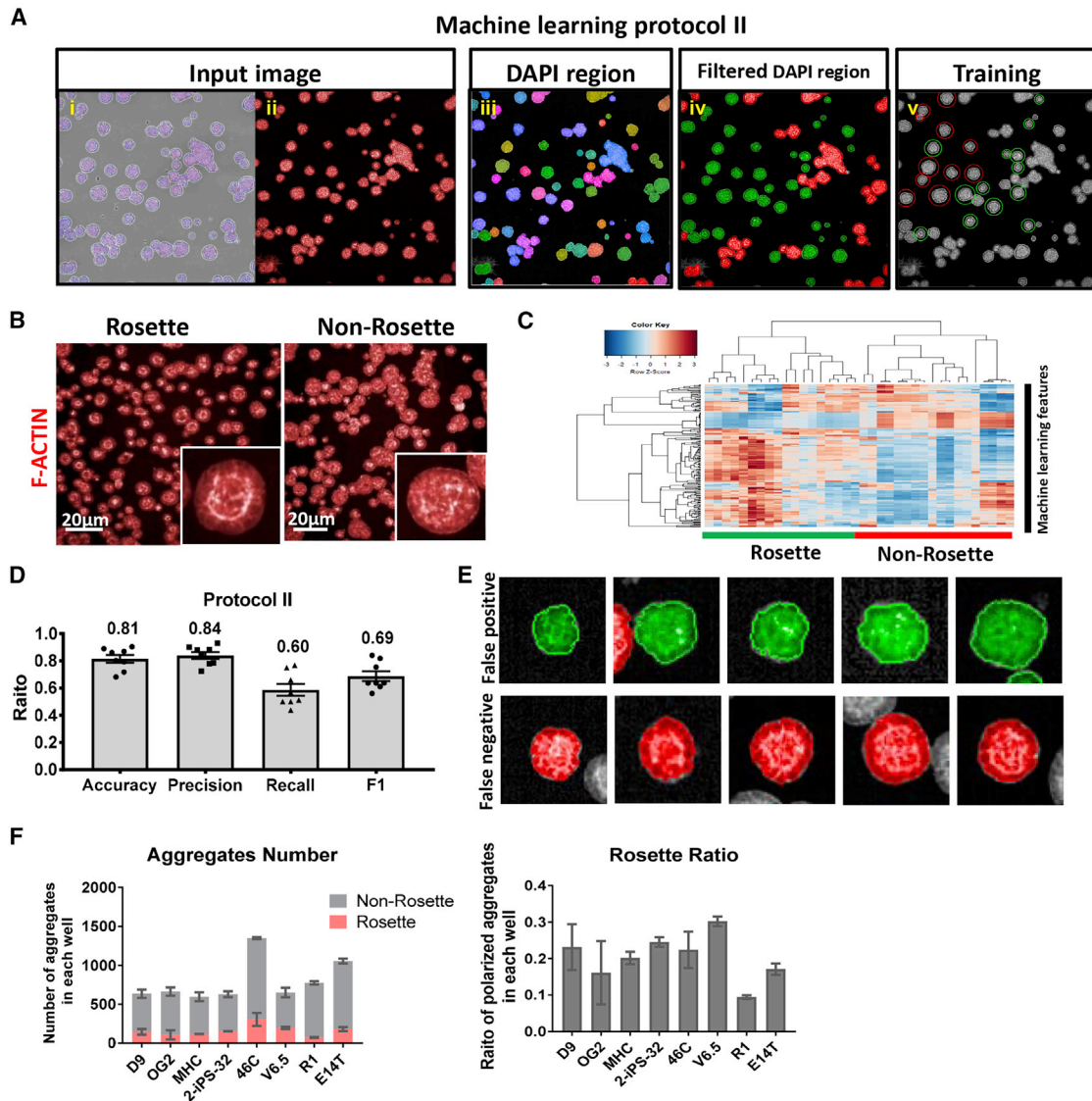


**Figure 3. Machine learning protocol II for evaluating polarization capacity**

(A) Images showing the process of machine learning protocol II. In the “iv. Filtered DAPI region,” the green structures were selected for downstream analyses; red structures were filtered out and excluded for analysis; the green and red circles in the “v. Training” panel mark the input rosette and non-rosette examples for training, respectively.

(B) Example images showing EBs with higher (rosette) and lower (non-rosette) polarization ability when cultured in 3D with Matrigel at day 4. Red, F-actin showing polarity. Scale bars, 20  $\mu\text{m}$ .

(C) Heatmap showing 204 machine learning features used for separate rosette and non-rosette EBs cultured in (B).

(D) Evaluation of the performance of machine learning protocol II. The value of accuracy, precision, recall, and F1 are indicated.

(E) Images showing false-positive and false-negative examples of machine learning protocol II. Green- and red-stained structures are high- and low-grade ITS recognized by machine learning;  $n = 1,328$  from 8 independent wells.

(F) Different polarization abilities of PSC lines when cultured with the 3D-on-top method in Matrigel on day 4. Lines and columns are means  $\pm$  SEM. Mean = 1,271, 1,327, 1,195, 1,259, 2,699, 1,303, 1,550, and 2,110 aggregates for D9, OG2, MHC, 2-iPS-32, 46C, V6.5, R1, E14T lines.  $N = 2$  separate experiments.

melatonin, rapamycin, LY294002, DKK1, BMP4, and metformin) scored significantly higher on multiple features than the DMSO control (Figure S5B). We used another

two ESC lines, E14T and 46C, to verify the seven candidates (Figures S5C and S5E). In the E14T line, all the candidates increased the high-grade ETS number, but LY294002 did

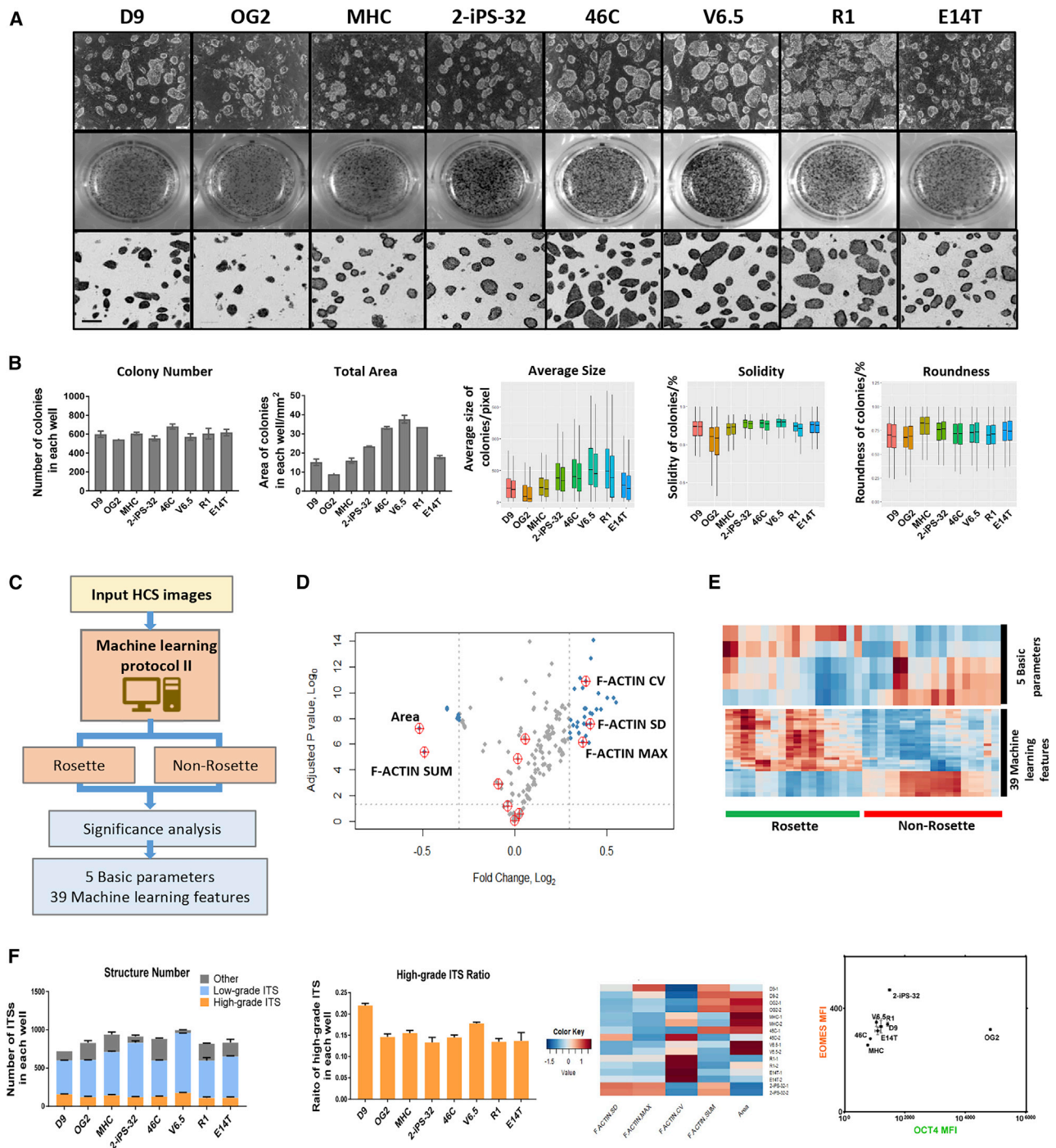


**Figure 4. Evaluating different mouse PSC lines by multi-parameters**

(A) Mouse PSC lines (iPSC: D9, OG2, MHC, 2-iPS-32; ESC: 46C, V6.5, R1, E14T) showed morphological differences when seeded as single cells in 2D culture. Scale bars, 50  $\mu$ m. The upper part shows PSC colonies under bright field. The middle and lower parts are the alkaline phosphatase staining of iPSC and ESC colonies on day 4.

(B) Quantification of colony number, total area, size, solidity, and roundness of different PSC lines. Columns are means  $\pm$  SEM. Boxes are median  $\pm$  interquartile. The mean colony numbers are 1,199, 1,089, 1,210, 1,110, 1,362, 1,141, 1,210, and 1,234 single colonies from D9, OG2, MHC, 2-iPS-32, 46C, V6.5, R1, and E14T PSC lines. N = 2 separate experiments.

(legend continued on next page)



not increase the high-grade ETS ratio; DKK1 decreased OCT4 MFI; and metformin and rapamycin appeared to inhibit polarization (Figures 5G and 55F). In the 46C line, LY294002 reduced high-grade ETS number and ratio; rapamycin decreased EOMES MFI; LY294002, melatonin, metformin, and rapamycin also inhibited polarization capacity (Figures 5G and 55F). The above results suggested a cell line-dependent effect of some candidates. Among all the cell lines tested, BMP4 increased the total high-grade ITS number, ratio, and polarity. BMP4 increased most the high-grade ITS number (1.39-fold) of the 46C line, and the ratio and polarization capacity (1.20- and 1.31-fold, respectively) of the D9 line (Figure 5G).

We focused on BMP4 for subsequent optimization, including the treatment time window and concentration (Figures 55C and 55D). Based on machine learning-assisted HCS 3D image analysis, BMP4 addition consistently increased the number of high-grade ITS (1.2- to 1.7-fold), while showing a dosage- and time window-dependent influence on ITS ratio and polarization capacity. Treatment at 25 ng/mL produced the highest ratio of high-grade ITSs (1.1- to 1.4-fold), while previous polarization capacity (1.14- to 1.5-fold) appeared under treatment on day 3 at any concentration (Figures 5G and 55G). We also characterized individual ITS embryos with or without BMP4 treatment based on 3D reconstructed images scanned by the 20× objective of the HCS system, which enabled us to recognize the nucleus (DAPI staining) and cell boundary (F-actin staining) (Figure 5H). The total cell number and ratio of TSCs/iPSCs in a single ITS embryo is similar in control and BMP4-treated groups. In contrast, BMP4-treated ITS embryos are more polarized and have significantly higher-quality iPSCs and TSCs (Figure 5I).

Finally, we tested whether ITS embryos can trigger a decidual reaction *in vivo* (Figure S6A). Polarized high-grade ITS embryos were selected and transferred into the uterus of pseudopregnant female mice (Figure S6B). On average, four deciduae can be seen in each uterus transferred with BMP4-treated ITS embryos. A uterus transferred with untreated ITS embryos had only one decidua (Figure S6C).

HE staining of uterine sections revealed that more blood cells surround the BMP4-treated ITS embryos (Figure S6D). This observation suggests that BMP4 may have enhanced the developmental potential of ITS embryos, subsequently leading to better crosstalk between ITS embryos with the uterus stroma, as reflected by the increase in the local vascular permeability. The above results support the notion that machine learning-assisted HCS can help identify factors that promote ITS embryo formation and development.

### Gene expression analysis of BMP4-treated ITS embryos

Finally, we performed transcriptional profiling of the iPSC or TSC compartments of the ITS embryo (ITS-iPSC or ITS-TSC) and individual iPSC or TSC aggregates (Figure 6A). A heatmap showed that pluripotency genes (*Pou5f1*, *Nanog*, and *Tdgf1*) were more highly expressed in both iPSC-alone and ITS-iPSC, while the *Cdx2* level was increased in TSC-alone and ITS-TSCs (Figure 6B). BMP4 upregulated general epiblast and primitive streak genes (*T*, *Wnt3*, and *Nodal*) as well as its target genes (*Id1* and *Id2*) in both iPSC-alone and ITS-iPSCs (Figure 6B). Principal-component analysis showed that BMP4 caused an apparent change in the transcriptome of iPSC-alone, TSC-alone, and ITS embryo (Figure 6C). We identified four distinct patterns of gene clusters (a complete gene ontology [GO] list can be found in Tables S1 and S2). Genes in cluster I were most highly expressed in BMP4-treated ITS-iPSCs (Figure 6D). The prominent gene groups in cluster I include histone modification, *in utero* embryonic development, actin regulation, gastrulation, cell polarity, etc. (Figure 6E). Cluster II genes showed the opposite trend as cluster I genes (Figure 6D). Genes involved in non-coding RNA (ncRNA) metabolism, stem cell maintenance, HIF-1, and p53 pathways are highly represented in cluster II genes (Figure 6E). Cluster III genes were most highly expressed in BMP4-treated iPSCs, and the cell polarity genes, histone modification, and ncRNA metabolism genes were higher in cluster III (Figures 6D and 6E). Cluster IV genes were more highly expressed in ITS-iPSC cells than in other groups (Figure 6D). They shared several similar GOs with cluster I and were enriched with

(C) Schematic of HCS data analysis workflow to distinguish polarization ability. A total of 204 features distinguished by machine learning protocol II were used to separate *rosette* and *non-rosette* structures. Five basic parameters and 39 machine learning features passed significance analysis between rosette and non-rosette structures were selected to distinguish polarization ability.

(D) Volcano plot showing significance analysis of all features and parameters between rosette and non-rosette EBs cultured in 3D outputted by HCS analysis. Dots show machine learning features; red circle shows basic parameters; gray dashed line marks the threshold ( $p < 0.05$ ,  $\log_2$  fold change  $> 0.3$ ); blue marks features or parameters with a significant difference between *rosette* and *non-rosette* EBs.

(E) Heatmap comparing the polarity of EBs using five representative basic parameters (Area, F-ACTIN SUM, F-ACTIN CV, F-ACTIN SD, F-ACTIN MAX) and 39 machine learning features that show a significant difference between rosette and non-rosette EBs.

(F) Quantification of high-grade ITS number, ratio, polarity ability, and OCT4/EOMES expression level on day 3 generated from different PSC lines. Gray columns (other) show structures failed to be distinguished by machine learning. MFI, mean fluorescent intensity. Columns/dots and lines are means  $\pm$  SEM. Mean = 319, 244, 292, 243, 257, 355, 223, and 227 from D9, OG2, MHC, 2-iPS-32, 46C, V6.5, R1, and E14T PSC lines. N = 2 separate experiments.

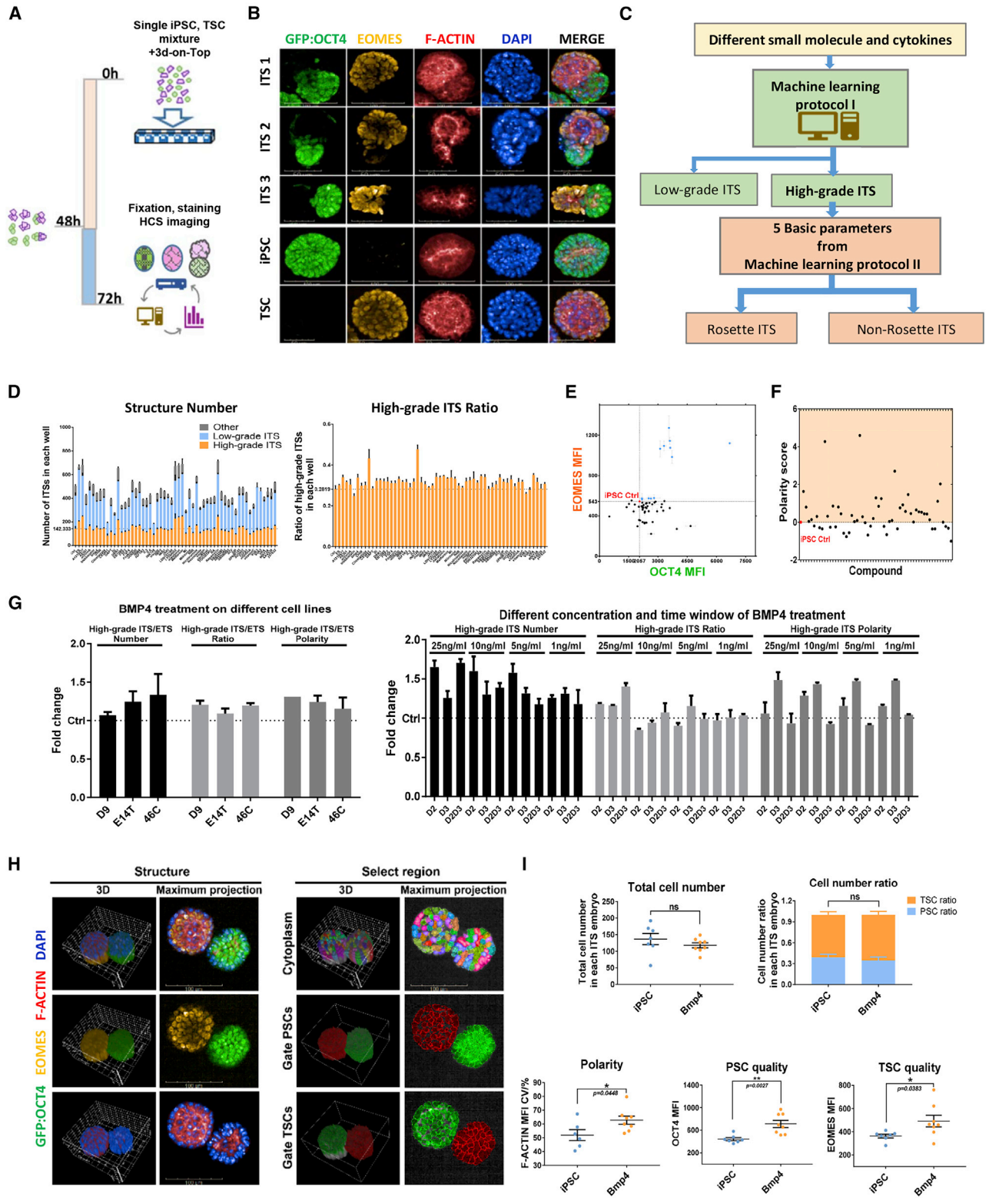


**Figure 5. High-content screening of small molecules and cytokines identified BMP4 as a potent inducer of ITS embryo morphogenesis**

(A) Schematic of small-molecule and cytokine screens on ITS embryos.

(legend continued on next page)



stem cell maintenance, ncRNA metabolism, HIF-1, and p53 signaling pathway genes (Figure 6E). Many key gastrulation regulators, members of mitogen-activated protein kinase, transforming growth factor  $\beta$ , Wnt signaling pathways, histone modification regulators, as well as genes regulating cell polarity and cytoskeleton, were found in cluster I (Figure 6F). Moreover, BMP4 treatment increased active transcription histone mark H3K4me3 on promoter regions of *Wnt3*, *Hand1*, *Fgfr1*, and *Tfap2b* (Figure 6G). Besides, BMP4 or TSC contact could upregulate pattern specification, embryonic organ development, or Hippo signaling pathway genes in iPSCs (Figures S7A–S7C).

We also compared the transcriptome of TSC-alone, ITS-TSC, BMP4-treated TSC-alone, and ITS-TSCs, and identified three major gene clusters (Figure 7A, for a complete GO list see Tables S3 and S4). Cluster I contained genes most highly expressed in ITS-TSCs or BMP4-treated ITS-TSCs, including mitochondrial respiratory chain complex assembly, ribosome biogenesis, DNA repair, cell cycle, and ncRNA metabolic process genes (Figure 7B). TSC cluster II genes were most highly upregulated by BMP4, with GO terms of chromosome segregation and DNA replication, suggesting that BMP4 may have promoted TSC proliferation (Figures 7A and 7B). TSC cluster III genes have the opposite trend as cluster I, and the autophagy genes were enriched (Figures

7A and 7B). BMP4 treatment or joining to iPSCs increased the expression level of many critical regulators of trophoblast cell and ExE growth and differentiation, such as *Esrrb*, *Eomes*, *Cdx2*, *Tead4*, and *BMP4* (Figure 7C). This trend aligns with our GO analysis that BMP4 induced cell-cycle- and cell division-related genes in TSCs. However, BMP4 also reduced the level of several trophoblast lineage markers *Krt8*, *Ascl2*, *Gata2*, *Ndr1*, and *Tfap2c*, suggesting that it may inhibit specific lineage of trophoblast development (Figure 7C). In summary, BMP4 seemed to exert an overall beneficial effect on both iPSC and TSC compartments to promote the polarization and gastrulation process in ITS embryos.

## DISCUSSION

Our study used machine learning-assisted HCS to investigate stem cell-based embryogenesis *in vitro*. We established robust, unbiased, and automated machine learning-based protocols to analyze the ability of multiple iPSC and ESC lines abilities to form ITS embryos, identify favorable conditions for ITS embryo generation, and perform cytokine and small-molecule screening to find factors that can promote ITS embryo generation. We

(B) Representative images of ITS embryo, iPSC-alone, and TSC-alone structures obtained on the HCS system using a 20  $\times$  water objective. Green, OCT4; yellow, EOMES; red, F-actin; blue, DAPI. Scale bar, 50  $\mu$ m.

(C) Schematic of HCS data analysis strategy based on machine learning to characterize ITS generated from different compound treatments. High-grade ITSs were further characterized by human selected parameters, including PSC quality (OCT4 MFI), TSC quality (EOMES MFI), and polarization ability (Area, F-ACTIN SUM, CV, SD, and MAX as in Figure 4D).

(D) Quantification of structure number and high-grade ITS ratio on day 3. Gray columns (other) show structures failed to be distinguished by machine learning. Lines and columns are means  $\pm$  SEM. N = 3 separate experiments. In total, 23,165 ITS embryos from 55 different treatment groups and 2 control groups.

(E) Scatterplot showing the OCT4 and EOMES expression level in the PSC and TSC parts from high-grade ITSs treated with different small molecules, respectively. Red marks the control ITS generated with iPSCs (D9) without any small-molecule treatment. Blue marks the small molecules improved the OCT4 and EOMES expression. Lines and dots are means  $\pm$  SEM. N = 3 separate experiments. In total, 23,165 ITS embryos from 55 different treatment groups and 2 control groups.

(F) Scatterplot showing the polarity score of high-grade ITSs treated with different small molecules. Red marks the high-grade ITSs generated with D9 iPSCs without any small-molecule treatment (control). The dashed line marks the polarity score of control high-grade ITSs. Polarity score was calculated by formula  $\text{SUM}_{\text{polarity factors}}[\log_2(\text{treatment}/\text{ctrl}) \times \text{weight}(\text{p value}/\text{fold change})]$ ; polarity factors: F-ACTIN SD, F-ACTIN MAX, F-ACTIN CV, F-ACTIN SUM, Area. Results pooled from 3 separate experiments. In total, 23,165 ITS embryos from 55 different treatment groups and 2 control groups.

(G) BMP4's effect on different cells and of different concentration/time window. Summary data from Figure S5F–G. Value mean  $\pm$  SEM is indicated on the graph. n = 96, 116, 120, 134, 115, 105, 117, and 107 for E14T line; n = 80, 92, 111, 92, 74, 114, 89, and 135 for 46C line; n = 140, 177, 232, 238, 184, 226, 194, 185, 220, 164, 183, 176, and 167 for different BMP4 concentrations and time windows at day 3. N = 2 separate experiments.

(H) Example of ITS 3D images obtained on the HCS system using a 20  $\times$  water objective. Left panel: 3D volume rendering images and maximum projection images. Green, OCT4; yellow, EOMES; red, F-actin; blue, DAPI. Scale bar, 100  $\mu$ m. Right panel, individual cells were identified and differentially colored based on DAPI/F-actin staining. iPSC or TSC parts can be separated through gating OCT4 or EOMES staining. The software can count the total cell number, epiblast cell number, or TSC number.

(I) Based on 3D reconstructed images obtained using the 20  $\times$  water objective, quantification of cell number, the polarity (F-ACTIN CV), and PSC/TSC quality of single ITS embryos with or without BMP4 treatment. (eight BMP4-treated and seven non-treated ITS embryos from three separate experiments). Two-sided Student's t test. Columns are means  $\pm$  SEM.

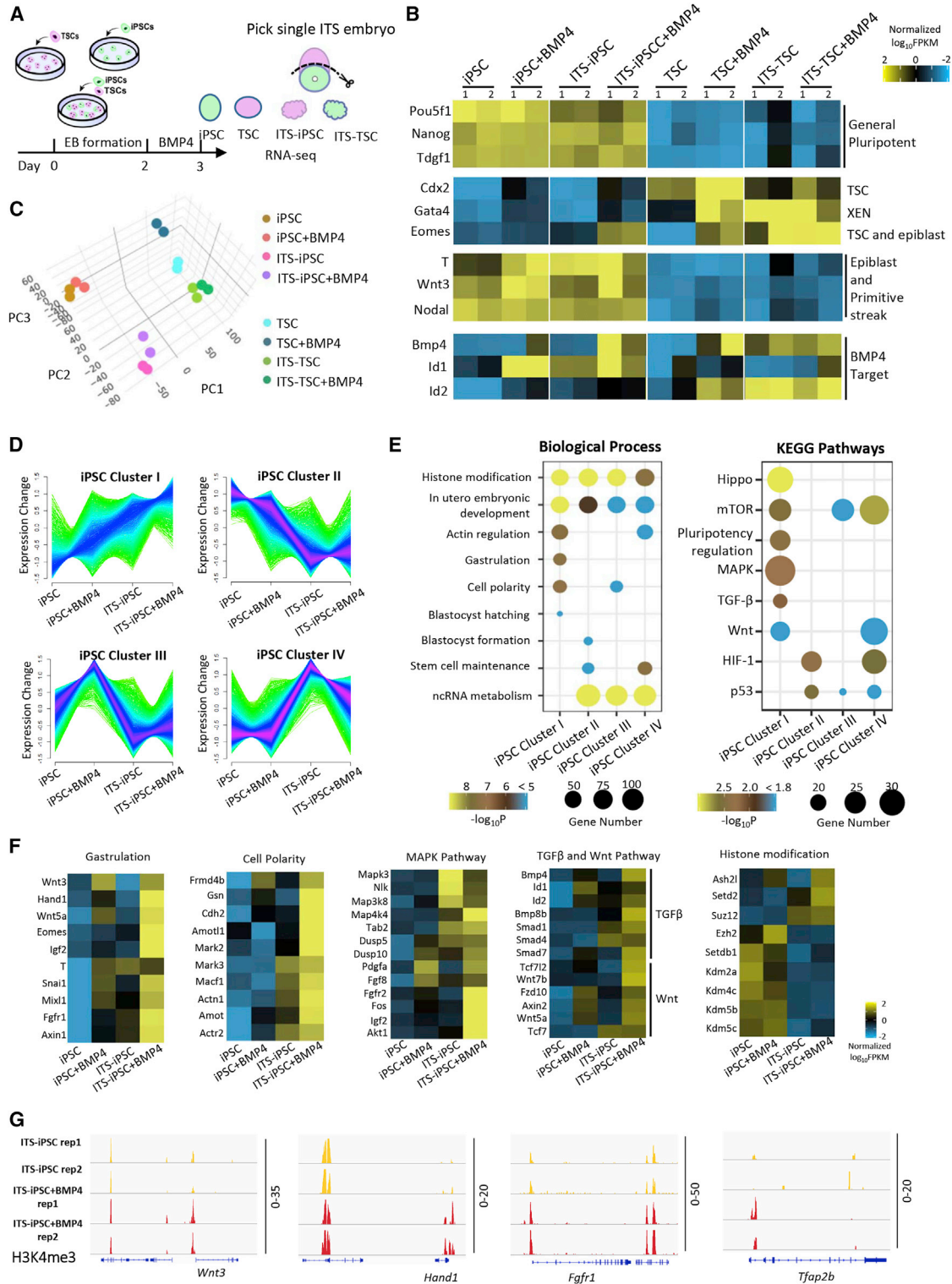


**Figure 6. Transcriptome analysis of the iPSC part in single ITS**

(A) Schematic of ITS embryo formation and RNA-seq sample collection procedure.

(B) Heatmap showing that iPSC, TSC, iPSC, and TSC parts of the ITS embryo expressed typical lineage marker genes and target genes of BMP4 signaling. Z score normalized  $\log_2$  FPKM value of each gene was used.

(legend continued on next page)

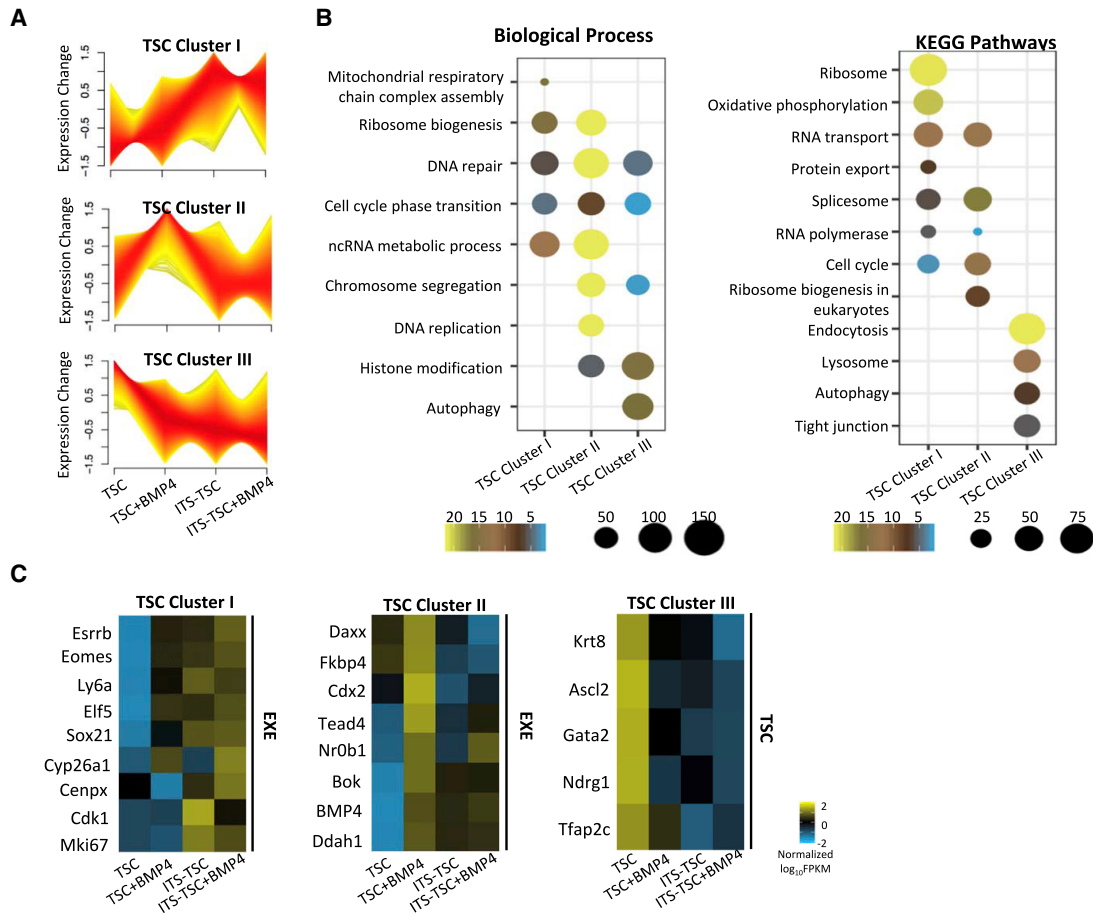


**Figure 7. Transcriptome analysis of the TSC part in single ITS**

(A) Mfuzz gene clustering analysis for TSC only and the structure-TSC part with or without BMP4 induction. x axis, different groups as labeled; y axis, gene expression level in normalized count value. Three distinct TSC cluster patterns were classified by Mfuzz (R package). (B) GO analysis of the three gene clusters in (A). The color represents the statistical significance calculated in logP. Yellow, higher p value; blue, lower p value. The size of the bubble represents the number of genes in each GO class. (C) Heatmap showing the expression level of trophectoderm marker genes in different TSC groups.

reveal the variation among different iPSC and ESC lines in forming embryo-like structures when mixed with TSCs. These approaches and findings are highly informative and relevant if one wants to study the morphogenesis ca-

capacity of human iPSCs and ESCs, which have different genetic backgrounds.

In traditional high-content analysis, researchers often choose a few basic parameters to score cell-specific traits.

(C) Principal-component analysis graph compares the transcriptome of non-treated and BMP4-treated single iPSC, TSC, iPSC, and TSC parts of the ITS embryo.

(D) Mfuzz gene clustering analysis of iPSC only and the ITS-iPSC part with or without BMP4 induction. x axis, different groups as labeled: iPSC only, iPSC plus BMP4, ITS-iPSC, and ITS-iPSC plus BMP4; y axis, gene expression level in normalized count value. Four distinct gene cluster patterns were classified by Mfuzz (R package).

(E) Gene ontology (GO) analysis of the four gene clusters in (D). The color represents the statistical significance calculated in logP. Yellow, higher p value; blue, lower p value. The size of the bubble represents the number of genes in each GO class. The larger bubble indicates more genes.

(F) Heatmap showing the expression level of selective developmental genes, signaling pathway, and histone modification genes in different iPSC groups.

(G) The UCSC browser snapshots showing histone H3K4me3 peaks at the promoter region of *Wnt3*, *Hand1*, *Fgfr1*, and *Tfap2b*. The scales represent the normalized reads counts.



As stem cell-based embryos are complex 3D structures, more comprehensive and unbiased parameter or feature selection will be necessary. We extracted a total of 228 features from high-content images of ITS structures and 204 features from rosette structures, far exceeding previously published studies (Table S8). A larger number of multivariate features helps to achieve more accurate classification of ITS embryos with unique and sophisticated morphology, and gives more robust statistical power. Moreover, our accuracy, precision, recall, and F1 scores were higher than most published papers using machine learning technology for image analysis (Table S8), indicating that our machine learning protocols performed satisfactorily. We used our machine learning protocols to analyze more than a million structures, to score for ITS embryos, rosette structures, and ITS embryos with rosette embryonic parts, which would not be possible with the human eye.

Compared with organoid or embryoid systems using only one type of stem cells, the ITS system is more challenging as it has two stem cell types (iPSC/ESCs and TSCs). Thus iPSCs/ESCs, TSCs, and the interaction between them will be differentially affected by small-molecule and cytokine treatment, not to mention the different concentrations and treatment window. One advantage of our machine learning platform is that, after setting up and validating machine learning protocols I and II, modules in each protocol, can be “mix and matched” to perform different comparisons and quantifications in an automated and highly efficient manner, and give unbiased and statistically significant results. With this powerful new platform, we showed that, among 55 factors, BMP4 performed the best overall and in different PSC lines. Our single ITS transcriptome analysis, H3K4me3 chromatin immunoprecipitation sequencing, and transfer experiments confirmed the positive effect of BMP4 on ITS formation and morphogenesis. Our results are consistent with known functions of BMP4 in anterior visceral endoderm (AVE), trophectoderm (TE), and TSCs (Kumar et al., 2018; Rivron et al., 2018; Tam et al., 2006); and in hESCs to promote gastrula-like structure formation *in vitro* (Warmflash, 2017). Interestingly, when both TSCs and BMP4 are present, the iPSC transcriptome became more similar to the embryonic part of an early gastrula embryo. Other factors that showed beneficial effects toward some aspects of ITS formation are also interesting candidates. Some of them may be combined to see whether a better phenotype can be achieved. For example, DKK1 treatment gave the best polarity score. It would be interesting to add BMP4 and DKK1 simultaneously, but this could confound the mechanism study.

Our machine learning protocols were established using the PhenoLOGIC machine learning software package, which provides a collection of machine learning algorithms to perform multi-feature analysis. Therefore, it reduces the

bias generated by a few machine learning algorithms developed by one group. It can also be easily adapted by other researchers to repeat our results or to perform screening on other state-of-art model systems, such as blastoid (Rivron et al., 2018), gastruloid (Beccari et al., 2018; Turner et al., 2017; Van den Brink et al., 2014), human epiblast-like structures with anteroposterior patterning (Martyn et al., 2018; Simunovic et al., 2019; Warmflash et al., 2014), and human or mouse PSC differentiation in microengineered chips or micropatterns (Morgani et al., 2018; Shao et al., 2017a; Xue et al., 2018). As PSCs and TSCs are more amenable to large-scale culture and genetic manipulation, CRISPR technology-based genetic screening using inducible knockout (iCRISPR) (González et al., 2014) or activation (idCas9-VPR) (Guo et al., 2017), combined with machine learning-assisted HCS, may be a robust approach to identify new regulators of mammalian embryo development through the stem cell-based embryo models.

In summary, machine learning-assisted high-content 3D image analysis could accelerate the exploration of the stem cell-based embryo models as well as other organoid systems. In the future, CRISPR-based genetic screen and bioengineering technologies could be incorporated to facilitate the generation of better PSC-derived models and possibly tissue-specific progenitor cells for regenerative medicine.

## EXPERIMENTAL PROCEDURES

For more details of this section, please also refer to the [supplemental experimental procedures](#).

In brief, to generate ITS/ETS embryos using PSCs and TSCs on Matrigel, we used a protocol similar to the one described in Harrison et al. (2017). In brief, PSCs and TSCs were dissociated to single cells and mixed at a 1:1 ratio or as otherwise mentioned. Optical-grade tissue culture dishes were covered with 60  $\mu$ L of liquid Matrigel, then allowed to solidify at 37°C before cells were seeded on top at  $1 \times 10^5$  cells/mL. The culture dishes were filled with the ETS medium containing 5% Matrigel. The ETS medium was changed every day without Matrigel supplement.

A Leica SP8 confocal with a water-immersion 25 $\times$  objective was used for individual ITS or ITX imaging. PerkinElmer Opera HCS machine was used for high-throughput and high-content image acquisition in a 48-well plate (Corning) with a 10 $\times$  or 20 $\times$  objective in confocal mode. ImageJ and PerkinElmer Opera software were used to analyze confocal images and high-content images, respectively.

For small-molecule and protein factor screening, mouse PSCs and TSCs were dissociated and mixed at a 1:1 ratio with a density of  $1 \times 10^5$  cells/mL. Forty-eight-well plates were pre-coated with 20  $\mu$ L Matrigel and then seeded with 500  $\mu$ L cell suspension in ITS/ETS medium containing 5% Matrigel per well. The plates were then incubated at 37°C for 24 h and replaced with the fresh medium the next day for another 24 h. Forty-eight hours after cell seeding, small molecules were added during ITS/ETS medium change. The structures were incubated with small molecules



for another 24 h, then fixed and stained, and scanned on a PerkinElmer Opera Phenix High-Content Screening System using the confocal mode. The image analysis strategy was developed using predefined building blocks and machine learning algorithms (PhenoLOGIC from Harmony software, PerkinElmer). For detailed analysis methods and sequences, see [supplemental information](#). The concentration of small molecules is listed in [Table S7](#).

Data are presented as mean  $\pm$  standard error of the mean or median  $\pm$  interquartile as indicated in the figure legend. Statistical significance was determined by Student's *t* test (two-tailed) for two groups using GraphPad software.  $p < 0.05$  was considered significant.

### Data and code availability

The RNA high-throughput sequencing data are publicly available at the National Center for Biotechnology Information with Gene Expression Omnibus, accession no. GSE 139379. The algorithms developed by this study are listed in the [supplemental information](#).

### SUPPLEMENTAL INFORMATION

Supplemental information can be found online at <https://doi.org/10.1016/j.stemcr.2021.03.018>.

### AUTHOR CONTRIBUTIONS

J.G., P.W., M.Z.-G., and J.N. conceived the study and designed experiments. J.G. performed mouse PSC, ESC, TSC, and XEN cell culture, ITX/ETX and ITS/ETS embryo assembly and characterization, HCS, and image analysis. J.G., P.W., and Y.Z. performed single iPSC, TSC, and ITS-iPSC, ITS-TSC structure collection, RNA-seq library construction, and data analysis. B.S. performed ETX and ETS embryo assembly experiments. H.Q. and X.Z. assisted with HCS data analysis and graphic presentation. J.G., P.W., and J.N. wrote the manuscript.

### DECLARATION OF INTERESTS

The author declare that they have no competing interests.

### ACKNOWLEDGMENTS

This work was supported by the National Key R&D Program of China (grants 2017YFA0102802 and 2019YFA0110001) to J.N., Wellcome Trust (098287/Z/12/Z, 108438/C/15/Z) and Curci Foundation grants to M.Z.-G., an NSFC grant (32000610) to J.G. J.G. is supported by postdoctoral fellowships from Tsinghua-Peking Center for Life Sciences. We thank Dr. P. Liu and Professor S. Ding from the School of Pharmaceutical Sciences, Tsinghua University, Beijing, China, for the mouse iPSC lines. Mingyao Cui from the Institute of Molecular Medicine, Peking University, Beijing, China, for assistance in RNA-seq experiments.

Received: October 20, 2020

Revised: March 17, 2021

Accepted: March 17, 2021

Published: May 11, 2021

### REFERENCES

- Beccari, L., Moris, N., Girgin, M., Turner, D.A., Baillie-Johnson, P., Cossy, A.C., Lutolf, M.P., Duboule, D., and Arias, A.M. (2018). Multi-axial self-organization properties of mouse embryonic stem cells into gastruloids. *Nature* 562, 272–276.
- Bedzhov, I., and Zernicka-Goetz, M. (2014). Self-organizing properties of mouse pluripotent cells initiate morphogenesis upon implantation. *Cell* 156, 1032–1044.
- Boutros, M., Heigwer, F., and Laufer, C. (2015). Microscopy-based high-content screening. *Cell* 163, 1314–1325.
- Czerniecki, S.M., Cruz, N.M., Harder, J.L., Menon, R., Annis, J., Otto, E.A., Gulieva, R.E., Islas, L.V., Kim, Y.K., Tran, L.M., et al. (2018). High-throughput screening enhances kidney organoid differentiation from human pluripotent stem cells and enables automated multidimensional phenotyping. *Cell Stem Cell* 22, 929–940 e924.
- Deglincerti, A., Croft, G.F., Pietila, L.N., Zernicka-Goetz, M., Siggia, E.D., and Brivanlou, A.H. (2016). Self-organization of the in vitro attached human embryo. *Nature* 533, 251–254.
- González, F., Zhu, Z., Shi, Z.-D., Lelli, K., Verma, N., Li, Q.V., and Huangfu, D. (2014). An iCRISPR platform for rapid, multiplexable, and inducible genome editing in human pluripotent stem cells. *Cell Stem Cell* 15, 215–226.
- Guo, J., Ma, D., Huang, R., Ming, J., Ye, M., Kee, K., Xie, Z., and Na, J. (2017). An inducible CRISPR-ON system for controllable gene activation in human pluripotent stem cells. *Protein Cell* 8, 379–393.
- Harrison, S.E., Sozen, B., Christodoulou, N., Kyprianou, C., and Zernicka-Goetz, M. (2017). Assembly of embryonic and extraembryonic stem cells to mimic embryogenesis in vitro. *Science* 356, eaal1810.
- Harrison, S.E., Sozen, B., and Zernicka-Goetz, M. (2018). In vitro generation of mouse polarized embryo-like structures from embryonic and trophoblast stem cells. *Nat. Protoc.* 13, 1586–1602.
- Kumar, R.P., Ray, S., Home, P., Saha, B., Bhattacharya, B., Wilkins, H.M., Chavan, H., Ganguly, A., Milano-Foster, J., Paul, A., et al. (2018). Regulation of energy metabolism during early mammalian development: TEAD4 controls mitochondrial transcription. *Development* 145, dev162644.
- Li, R., Zhong, C., Yu, Y., Liu, H., Sakurai, M., Yu, L., Min, Z., Shi, L., Wei, Y., and Takahashi, Y. (2019). Generation of blastocyst-like structures from mouse embryonic and adult cell cultures. *Cell* 179, 687–702. e618.
- Liu, P., Chen, M., Liu, Y., Qi, L.S., and Ding, S. (2018). CRISPR-based chromatin remodeling of the endogenous Oct4 or Sox2 locus enables reprogramming to pluripotency. *Cell Stem Cell* 22, 252–261 e254.
- Lukonin, I., Serra, D., Challet Meylan, L., Volkmann, K., Baaten, J., Zhao, R., Meeusen, S., Colman, K., Maurer, F., Stadler, M.B., et al. (2020). Phenotypic landscape of intestinal organoid regeneration. *Nature* 586, 275–280.
- Martyn, I., Kanno, T.Y., Ruzo, A., Siggia, E.D., and Brivanlou, A.H. (2018). Self-organization of a human organizer by combined Wnt and Nodal signalling. *Nature* 558, 132–135.



- Morgani, S.M., Metzger, J.J., Nichols, J., Siggia, E.D., and Hadjantonakis, A.K. (2018). Micropattern differentiation of mouse pluripotent stem cells recapitulates embryo regionalized cell fate patterning. *ife* 7, e32839.
- Poh, Y.-C., Chen, J., Hong, Y., Yi, H., Zhang, S., Chen, J., Wu, D.C., Wang, L., Jia, Q., and Singh, R. (2014). Generation of organized germ layers from a single mouse embryonic stem cell. *Nat. Commun.* 5, 4000.
- Rivron, N.C., Frias-Aldeguer, J., Vrij, E.J., Boisset, J.C., Korving, J., Vivie, J., Truckenmuller, R.K., van Oudenaarden, A., van Blitterswijk, C.A., and Geijsen, N. (2018). Blastocyst-like structures generated solely from stem cells. *Nature* 557, 106–111.
- Scheeder, C., Heigwer, F., and Boutros, M. (2018). Machine learning and image-based profiling in drug discovery. *Curr. Opin. Syst. Biol.* 10, 43–52.
- Shahbazi, M.N., Jedrusik, A., Vuoristo, S., Recher, G., Hupalowska, A., Bolton, V., Fogarty, N.M., Campbell, A., Devito, L.G., and Ilic, D. (2016). Self-organization of the human embryo in the absence of maternal tissues. *Nat. Cell Biol.* 18, 700.
- Shao, Y., Taniguchi, K., Gurdziel, K., Townshend, R.F., Xue, X., Yong, K.M.A., Sang, J., Spence, J.R., Gumucio, D.L., and Fu, J. (2017a). Self-organized amniogenesis by human pluripotent stem cells in a biomimetic implantation-like niche. *Nat. Mater.* 16, 419–425.
- Shao, Y., Taniguchi, K., Townshend, R.F., Miki, T., Gumucio, D.L., and Fu, J. (2017b). A pluripotent stem cell-based model for post-implantation human amniotic sac development. *Nat. Commun.* 8, 208.
- Shen, Y., Kubben, N., Candia, J., Morozov, A.V., Misteli, T., and Losert, W. (2018). RefCell: multi-dimensional analysis of image-based high-throughput screens based on 'typical cells'. *BMC Bioinformatics* 19, 427.
- Simunovic, M., Metzger, J.J., Etoc, F., Yoney, A., Ruzo, A., Martyn, I., Croft, G., You, D.S., Brivanlou, A.H., and Siggia, E.D. (2019). A 3D model of a human epiblast reveals BMP4-driven symmetry breaking. *Nat. Cell Biol.* 21, 900–910.
- Sozen, B., Amadei, G., Cox, A., Wang, R., Na, E., Czukiewska, S., Chappell, L., Voet, T., Michel, G., Jing, N., et al. (2018). Self-assembly of embryonic and two extra-embryonic stem cell types into gastrulating embryo-like structures. *Nat. Cell Biol.* 20, 979–989.
- Sozen, B., Cox, A.L., De Jonghe, J., Bao, M., Hollfelder, F., Glover, D.M., and Zernicka-Goetz, M. (2019). Self-organization of mouse stem cells into an extended potential blastoid. *Dev. Cell* 51, 698–712 e698.
- Tam, P.P., Loebel, D.A., and Tanaka, S.S. (2006). Building the mouse gastrula: signals, asymmetry and lineages. *Curr. Opin. Genet. Dev.* 16, 419–425.
- Turner, D.A., Girgin, M., Alonso-Crisostomo, L., Trivedi, V., Baillie-Johnson, P., Glodowski, C.R., Hayward, P.C., Collignon, J., Gustavsen, C., Serup, P., et al. (2017). Anteroposterior polarity and elongation in the absence of extra-embryonic tissues and of spatially localised signalling in gastruloids: mammalian embryonic organoids. *Development* 144, 3894–3906.
- Van den Brink, S.C., Baillie-Johnson, P., Balayo, T., Hadjantonakis, A.-K., Nowotschin, S., Turner, D.A., and Arias, A.M. (2014). Symmetry breaking, germ layer specification and axial organisation in aggregates of mouse embryonic stem cells. *Development* 141, 4231–4242.
- Veenvliet, J.V., Bolondi, A., Kretzmer, H., Haut, L., Scholze-Wittler, M., Schifferl, D., Koch, F., Guignard, L., Kumar, A.S., Pustet, M., et al. (2020). Mouse embryonic stem cells self-organize into trunk-like structures with neural tube and somites. *Science* 370, eaba4937.
- Warmflash, A. (2017). Synthetic embryos: windows into mammalian development. *Cell Stem Cell* 20, 581–582.
- Warmflash, A., Sorre, B., Etoc, F., Siggia, E.D., and Brivanlou, A.H. (2014). A method to recapitulate early embryonic spatial patterning in human embryonic stem cells. *Nat. Methods* 11, 847–854.
- Xue, X., Sun, Y., Resto-Irizarry, A.M., Yuan, Y., Aw Yong, K.M., Zheng, Y., Weng, S., Shao, Y., Chai, Y., Studer, L., et al. (2018). Mechanics-guided embryonic patterning of neuroectoderm tissue from human pluripotent stem cells. *Nat. Mater.* 17, 633–641.
- Zhang, S., Chen, T., Chen, N., Gao, D., Shi, B., Kong, S., West, R.C., Yuan, Y., Zhi, M., Wei, Q., et al. (2019). Implantation initiation of self-assembled embryo-like structures generated using three types of mouse blastocyst-derived stem cells. *Nat. Commun.* 10, 496.
- Zheng, Y., Xue, X., Shao, Y., Wang, S., Esfahani, S.N., Li, Z., Muncie, J.M., Lakins, J.N., Weaver, V.M., and Gumucio, D.L. (2019). Controlled modelling of human epiblast and amnion development using stem cells. *Nature* 573, 421–425. <https://doi.org/10.1038/s41586-019-1535-2>.